Available online at www.sciencedirect.com
ScienceDirect
Applied Catalysis B: Environmental 81 (2008) 14–26
APPLIED CATALYSIS B: ENVIRONMENTAL
www.elsevier.com/locate/apcatb

# Olivine catalysts for methane- and tar-steam reforming

John N. Kuhn [a], Zhongkui Zhao [a], Larry G. Felix [b], Rachid B. Slimane [c], Chun W. Choi [c], Umit S. Ozkan [a,*]

[a] *Department of Chemical and Biomolecular Engineering, The Ohio State University, 140 W. 19th Avenue, Columbus, OH 43210, USA*
[b] *Gas Technology Institute, 1500 First Avenue, North, Suite L134, Birmingham, AL 35203-1821, USA*
[c] *Gas Technology Institute, 1700 S. Mt. Prospect Road Des Plaines, IL 60618-1804, USA*

Received 22 June 2007; received in revised form 16 November 2007; accepted 30 November 2007
Available online 8 December 2007

**Abstract**

The removal of tar and lower hydrocarbons is a vital technological barrier hindering the development of biomass gasification. The present work evaluates four olivine catalysts (three untreated of different origin and one calcined) for lowering the amount of these compounds in biomass derived syngas by reforming model compounds (naphthalene, toluene, and methane). Treatments prior to reaction were shown to largely impact the catalytic activity and physiochemical properties of the olivine catalysts depending on its origin. The formation of free Fe phases following decomposition of a Fe-bearing serpentine phase ($(Mg,Fe)_3Si_2O_5(OH)_4$) near the surface of untreated olivine catalysts proved most important for facilitating higher activity compared to olivine catalysts with little or no serpentine phase initially. The most active catalyst was efficient at naphthalene removal (90% conversion at 800 °C), but more active catalysts are needed for applications where methane removal is required. Additionally, carbon deposition during naphthalene-steam reforming as well as Fe clustering during naphthalene-steam reforming and exposure to reducing conditions suggested stability may be a liability.


*Keywords:* Olivine catalyst; Tar removal; Biomass gasification; Catalyst activation; Catalytic stability

## 1. Introduction

Great interest exists to produce energy from renewable sources such as biomass. The U.S. could sustainably produce the equivalent of over half of its oil consumption ($3.8 \times 10^9$ of $7.0 \times 10^9$ barrels of oil per year) from biomass while still fulfilling its demands for domestic human consumption, livestock feed, and exportation [1]. Gasification is currently a leading option for converting biomass to fuel or chemicals since syngas utilization technologies are already proven [1]. A promising scheme is a fluidized-bed (FB) gasifier with steam as the oxidant. Compared to updraft or downdraft gasifiers, FB gasifiers represent a balance for potential large-scale applications, ability to handle wet biomass, low impurity formation, and high thermal efficiencies. Addition of a second zone for a two-stage or dual FB gasifier further increases efficiency and fuel quality [2,3]. In the first zone, biomass is gasified with steam while char and coke are combusted (to power the endothermic gasification) with air in the second zone to make flue gas. Additionally, biomass gasification is integral towards developing technologies such as fuel cells that need a supply of $H_2$ (produced directly from syngas or indirectly from $CH_3OH$). Before use as fuel or in chemical synthesis, syngas is purified via the water-gas reaction and further purification depends upon the use. For example, CO and hydrocarbon removal are needed before a polymer electrolyte membrane fuel cell (PEMFC) or $CH_3OH$ synthesis while the effluent could be directly fed to a solid oxide fuel cell (SOFC).

Regardless of use, the primary roadblock preventing biomass gasification commercialization is formation of tars [4]. Tars are a blend of single and polycyclic aromatic hydrocarbons and are generally described as any organic contaminant with a higher molecular weight than benzene [2]. Tars cause problems by condensing in piping and on filters and is also detrimental to downstream processing [5]. Costs associated with removing tars can be greater than overall project costs [4]. Minimization of tar formation by primary methods such as optimization of gasification conditions, by

* Corresponding author. Tel.: +1 614 292 6623; fax: +1 614 292 3769.
*E-mail address:* Ozkan.1@osu.edu (U.S. Ozkan).

0926-3373/$ – see front matter © 2007 Elsevier B.V. All rights reserved.
doi:10.1016/j.apcatb.2007.11.040

gasifier design, or by the use of in-bed catalytic additives is desirable [2]. Optimization of gasification conditions and gasifier design may not be enough to effectively reduce tars to desired levels. Additionally, optimization is not always possible. For example, biomass feedstocks have different optimum gasification temperatures that depend upon factors other than tar formation [2]. Moreover, gasifier design is not possible when an existing apparatus is available.

Several technologies are proven for tar removal, but are based on physical or secondary removal methods. Physical methods (e.g., wet scrubbing) are efficient, but generate large amounts of wastewater from which the tars must be separated and disposed. These methods are inefficient unless the gas is needed near ambient temperatures and also lead to decreased fuel value [5]. Consequently, it is desirable to clean the gas at elevated temperatures. Tar can also be removed by hot gas conditioning following the gasifier. Thermal cracking is precluded since temperatures (>1100 °C) higher than those used during gasification are required [5]. Tar reforming is an attractive method since it improves thermal integration and biomass utilization efficiency. Due to poor attrition resistance of current catalysts [5–7], two reactors are needed at the gasifier exit. In the first reactor, dolomite catalysts are used to prevent high concentrations of tar from reaching the second reactor where commercial Ni-based catalysts are used to reform remaining tars and lower hydrocarbons. The tar levels must be lowered significantly to protect the Ni-based catalysts from coking.

Development of an in-bed catalyst that could reform tar and $CH_4$ under gasification conditions would allow for elimination of the external reactors. Several other catalysts such as alkali metals (particle agglomeration, removal issues), precious metal (expensive), char (consumed during gasification), and clay minerals (unstable at high temperatures) are limited for the aforementioned reasons and are generally less active than Ni or dolomite catalysts [5–7]. Olivine catalysts are a promising alternative since they are inexpensive and attrition resistant [5–7]. Olivine is a silicate material containing hexagonally packed oxygen atoms. Tetrahedral holes (an eighth) are filled by Si while metals occupy half of the tetrahedral holes. In naturally formed minerals, Mg (forsterite) and Fe (fayalite) are the main occupants. Other metals (e.g., Mn, Cr, Co, and Ni) are present at low levels, but can be incorporated synthetically.

Olivine catalysts have been studied for steam and dry reforming of methane [8], steam reforming of toluene ($C_7H_8$) [9], and steam and dry reforming of naphthalene ($C_{10}H_8$) [10–12]. $C_7H_8$ and $C_{10}H_8$ are considered as surrogate tar compounds since they form at high levels. $C_{10}H_8$ is a good model compound because it is highly stable [7,11]. Moreover, olivine catalysts were used as a bed additive in FB steam gasifiers using crushed almond shells [13] and wood chips [14], in FB air gasifiers operating on a mixture of pine wood chips and olive oil residue [15], and in a secondary reactor processing the effluent from steam gasifier using beech as the biomass source [16]. These studies demonstrated that olivine is nearly as active as dolomite [13], 60% as active as dolomite [15], and mixed results depending upon temperature and the class of tar evaluated [16]. These differences were speculated to be caused by calcinations, which are not always stated [15]. It was also proposed that olivine catalysts from different origin should be evaluated [10]. Treatments of the Austrian olivine catalyst (note that sample was sintered in air at 1600 °C before evaluation) [17] under oxidizing and reducing conditions and the Norwegian olivine catalyst under oxidizing conditions [10–12] and under different syngas compositions [12] showed a substantial influence upon properties. Direct comparisons of gasification results [13,15,16] are not possible because of differences in oxidants, biomass sources, and olivine catalysts. No comparisons are available for fixed bed reactions for the similar reasons [8–12]. That is, a systematic study of olivine catalysts under similar conditions has not been performed.

The present work examines olivine catalysts of different origin and the effect of treatments upon the catalytic behavior and physiochemical properties. Olivine catalysts from Austria, North Carolina, and Washington are evaluated with an emphasis on relating activity differences for reforming of model compounds to property differences. Stability of the catalysts is also discussed. Results presented in this article focus on the catalytic and physicochemical differences in the support materials and constitute the first phase of a series of studies where Ni-olivine catalysts prepared by a thermal impregnation method are investigated.

## 2. Experimental

### 2.1. Catalyst details

Olivine samples were acquired from three different locations: Washington (Wash.), North Carolina (N.C.), and Austria. Each sample was acquired without chemical treatment. Samples were sized to 180–300 μm range (50–80 mesh) by mechanical treatments. Moreover, a second Austrian olivine sample was acquired following sintering in air at 1600 °C for 4 h. Austrian samples were acquired from Magnolithe GMBH Company while the domestic samples were acquired from Unimin Corporation through Reade Advanced Materials. Elemental analyses were performed using inductively coupled plasma mass spectrometry (ICP-MS) following the ASTM D-6349 analysis procedure.

### 2.2. Reaction testing

Catalytic activity was measured by three sets of reaction conditions: (i) simultaneous reforming of $C_{10}H_8$ and $C_7H_8$, (ii) reforming of $C_{10}H_8$, and (iii) $CH_4$-$H_2O$ reforming. Experimental parameters for the first two reactions were selected to closely mimic those prevailing in a biomass gasifier and results were previously reported elsewhere [18,19]. These reactions are described in the following text based on the aromatic compounds fed to the reactor. Gas flows were controlled using calibrated mass flow controllers. When both $C_{10}H_8$ and $C_7H_8$ were present, the composition was 20.5% $H_2$/20.5% CO/28.0% $CO_2$/23.5% $H_2O$/5.6% $CH_4$/balance $N_2$ with 2800 ppm $C_7H_8$ and 170 ppm $C_{10}H_8$. When $C_7H_8$ was not a reactant, the composition was 16.0% $H_2$/8.0% CO/12.0% $CO_2$/16.0% $H_2O$/

4.0% $CH_4$/balance $N_2$ with 400 ppm $C_{10}H_8$. Steam was generated using a metering pump to transport distilled water into a stainless steel coil located within a tube furnace. $C_{10}H_8$ and $C_7H_8$ were introduced using liquid pumps. In the case of reactions where $C_7H_8$ was not a reactant, $C_{10}H_8$ was fed by sparging $N_2$ through a 3 L stainless steel vessel held at 140 °C. Reactants were combined in a mixing chamber before being sent to the reactor. Lines were heated to 250 °C to prevent $C_{10}H_8$ crystallization. Catalysts were supported onto a porous frit in a quartz reactor and loaded on an equal volume basis (154.4 and 101.7 $cm^3$ when both $C_{10}H_8$ and $C_7H_8$ were fed and when only $C_{10}H_8$ was fed, respectively). In reactions involving both $C_{10}H_8$ and $C_7H_8$, the pressure and gas hourly space velocity (GHSV) were 5 bar and 2500 $h^{-1}$, respectively. When only $C_{10}H_8$ was a reactant, the pressure and GHSV were 1 bar and 1166 $h^{-1}$, respectively. Composition of gas streams were measured by gas chromatography (Varian micro GC or HP 3890) and FTIR. Calculations were made using the following definitions.

$$\%\text{reactant conversion} = 100\% \times \frac{(\text{moles converted})}{(\text{moles fed})}$$

$$\%C_6H_6\text{ yield} = 100\% \times \frac{(\text{moles of } C_6H_6 \text{ produced})}{(\text{moles of } C_{10}H_8 \text{ and } C_7H_8 \text{ fed})}$$

$$\%C_2H_4\text{ yield} = 100\% \times \frac{(\text{moles of } C_2H_4 \text{ produced})}{((5 \times \text{moles of } C_{10}H_8 \text{ fed}) + (3 \times \text{moles of } C_7H_8 \text{ fed}))}$$

$$\%H_2\text{ yield} = 100\% \times \frac{(\text{moles of } H_2 \text{ produced})}{((4 \times \text{moles of } C_{10}H_8 \text{ fed}) + (4 \times \text{moles of } C_7H_8 \text{ fed}) + (2 \times \text{moles of } CH_4 \text{ fed}) + (\text{moles of } H_2O \text{ fed}))}$$

$$\%CO\text{ yield} = 100\% \times \frac{(\text{moles of CO produced})}{((10 \times \text{moles of } C_{10}H_8 \text{ fed}) + (7 \times \text{moles of } C_7H_8 \text{ fed}) + (\text{moles of } CH_4 \text{ fed}) + (\text{moles of } CO_2 \text{ fed}))}$$

Activity was also monitored for $CH_4$-$H_2O$ reforming using temperature-programmed reactions on an equal mass basis. Catalysts were loaded into a U-tube quartz reactor between quartz wool plugs. The effluent was monitored with a Cirrus RGA mass spectrometer using the Faraday detector. Reactions were performed with 50 mL/min total flow containing 3% $CH_4$ and $H_2O$. Before the reaction, samples were reduced in 20% $H_2$/He at 600 °C for 2 h. During the reaction, the temperature was ramped (5 °C/min) from 600 °C (no activity observed below this temperature) to 900 °C, where it was held for 1 h. The temperature-program was repeated two additional times to monitor changes with time on stream.

### 2.3. Catalyst characterization

Mass specific BET surface area measurements were made at 77 K using a Micromeritics ASAP 2010 instrument. Kr was selected as the probe molecule because of the low surface areas (<5 $m^2$/g). Before analysis, samples were degassed overnight at 130 °C. Measurements were repeated within 3% difference.

Temperature-programmed reduction (TPR) and oxidation (TPO) were performed with a Micromeritics Autochem II 2920 equipped with a TCD. Catalysts (150 mg) were loaded into a quartz U-tube reactor and subjected to a pre-treatment in He (30 mL/min) at 900 °C (heated at 20 °C/min) for 10 min. After cooling to 40 °C, a TPR was performed in 10% $H_2$/Ar (30 mL/min) to 950 °C (15 °C/min). After cooling in He, a TPO was performed in 10% $O_2$/He (30 mL/min) to 950 °C (15 °C/min). The TPR/O cycle was then repeated. The TCD was calibrated for quantitative analyses using standards.

X-ray diffraction (XRD) patterns were acquired with a Bruker D8 Advance diffractometer equipped with a Braun position sensitive detector (8°). Spectra were obtained between 20 and 90° 2-$\Theta$ using Cu $K\alpha_1$ radiation (1.5406 nm) at 40 kV and 50 mA. For data under ambient conditions, a 9-sample holder attachment and rotating polypropylene sample holders were employed. In situ data were acquired with the HTK 1200 oven equipped with graphite windows. Samples were supported on an alumina holder with a 0.5 mm deep reservoir. The active gas, 5% $H_2/N_2$, was used at a flow rate of 10 mL/min. A heating rate of 10 °C/min and a 20 min hold time before scanning at each temperature were also employed. The International Center for Diffraction Data (ICDD) library was used for phase identification. The Xfit software package was used for peak fitting data. Lattice parameters were calculated using a least-squares analysis of fitted data.

Raman spectra were acquired with Horiba-Jobin Yvon LabRam HR Raman Microscope equipped with an internal He–Ne red laser (633 nm) and an 800 mm focal length spectrometer. Spectra were obtained with a power of 5 mW at the sample, the 1800 grating, and 50× long working distance objective. Acquisition number and time were altered depending on a given sample's scattering ability. At least 10 spectra were acquired for each sample to guarantee representative data.

Infrared spectra were acquired on a ThermoElectron Nicolet 6700 FTIR equipped with an ATR attachment and a MCT detector. Samples were loaded in a trough on a Zn–Se crystal floor. Spectra were acquired using 500 scans with a resolution of 4 $cm^{-1}$.

Thermal treatments under an inert atmosphere (30 mL/min of He) were monitored by a Thermo-Finnigan Trace Ultra differential scanning quadrupole (DSQ) gas chromatograph/mass spectrometer (GC/MS). Samples (100 mg) were loaded into a quartz U-tube reactor between quartz wool plugs, heated to 850 °C at 10 °C/min, and held there for 20 min. Data for the GC/MS were obtained using selected ion mode and a 3 eV detector gain.

XPS spectra were acquired under high vacuum using a Kratos Ultra Spectrometer. A monochromatic Al source at 13 kV and 10 mA was used in conjunction with analyzer mode,

hybrid lens mode, and a slot aperture setting. Samples were ground into carbon tape and degassed overnight before being loaded into the analyzer chamber. Samples were height optimized for maximum signal, corrected by C 1 s binding energy at 284.5 eV, and charge neutralized during acquisition with 2.1 A filament current, 1.3 V filament bias, and 2.3 V filament charge. Data were deconvoluted with Gaussian peaks using the software package XPS Peak 4.1. Linear backgrounds were used for all regions except Fe, which used a mixture of linear and Shirley-type backgrounds. Surface compositions were determined with transmission values and relative sensitivity factors for this instrument and an Al source.

## 3. Results

The influence of olivine's origin and the effect of treatments on the Austrian catalysts are discussed simultaneously and the results are presented by analysis technique. The most active catalyst (untreated Austrian) was also characterized following $C_{10}H_8$-$H_2O$ reforming for 2 days between 750 and 900 °C in order to assess stability.

### 3.1. Reaction studies

Reaction results between 800 and 900 °C for simultaneous reforming of $C_7H_8$ and $C_{10}H_8$ over the N.C. olivine catalyst are shown in Table 1. These data are representative of the product distribution over the other olivine catalysts examined in this work and also demonstrate the complexity of the reaction network. $C_7H_8$ was fed in $C_{10}H_8$ in much higher quantities, but showed comparable or higher conversions. These results confirmed that $C_{10}H_8$ is more difficult to remove than $C_7H_8$ [7,11]. Since $C_{10}H_8$ was more difficult to remove than $C_7H_8$ and olefinic products ($C_6H_6$, $C_2H_4$) were detected, the results agreed with previous studies that identified the loss of aromaticity as rate limiting [11]. $C_6H_6$ was produced from $C_7H_8$ and also likely from $C_{10}H_8$, which is consistent with previous results [12] that showed both $C_{10}H_8$ and $C_7H_8$ form $C_6H_6$ on the way to forming permanent gases. Conversion of $CH_4$ was low and conversions for $H_2$ and CO were between −0.1 (i.e., generation) and 0.1%. Both $H_2O$ and $CO_2$ were consumed during the reaction indicating that dry and steam reforming are operative in breaking down tars. Additionally, the water–gas shift reaction may help re-adjust the proportions of these species.

Table 1
Reaction results during simultaneous naphthalene and toluene reforming over the untreated N.C. olivine catalyst

| | 800 °C | 850 °C | 900 °C |
|---|---|---|---|
| Conversion (%) | | | |
| $C_{10}H_8$ | 33.4 | 77.1 | 100.0 |
| $C_7H_8$ | 70.1 | 88.3 | 89.4 |
| $CH_4$ | 0.0 | 0.0 | 0.6 |
| $H_2O$ | 1.0 | 1.0 | 1.0 |
| $CO_2$ | 2.0 | 4.1 | 9.1 |
| Yield (%) | | | |
| $C_6H_6$ | 54.1 | 50.7 | 35.0 |
| $C_2H_4$ | 0.0 | 0.0 | 0.2 |

*Conditions*: 20.5% $H_2$/20.5% CO/28.0% $CO_2$/23.5% $H_2O$/5.6% $CH_4$/ balance $N_2$ with 2800 ppm $C_7H_8$ and 170 ppm $C_{10}H_8$, GHSV = 2500 and $P$ = 5 bar.

Table 2
Naphthalene conversion for olivine catalysts as a function of temperature

| Catalyst | 750 °C | 800 °C | 850 °C | 900 °C |
|---|---|---|---|---|
| Wash. | 30 | 60 | 80 | 97 |
| N.C. | 40 | 75 | 85 | 98 |
| Austrian | 50 | 90 | 95 | 100 |
| Austrian-calcined | – | 32 | 62 | 92 |

*Conditions*: 16.0% $H_2$/8.0% CO/12.0% $CO_2$/16.0% $H_2O$/4.0% $CH_4$/balance $N_2$ with 400 ppm $C_{10}H_8$, GHSV = 1166, and $P$ = 1 bar.

Tar removal ability, as presented in Table 2, was measured in more simple studies where $C_{10}H_8$ was the only aromatic compound fed to the reactor. Both the origin of the olivine sample and reaction temperature played important roles. The trend in naphthalene conversion cannot be explained by surface area and density differences as shown in Table 3. For example, the catalyst with the highest surface area and highest density (Wash.) has the lowest $C_{10}H_8$ removal ability at all temperatures. Consequently, differences in the properties of these catalysts led to a range of conversion that spanned from 60 to 90% at 800 °C.

In addition to the three samples presented in Table 2, a Norwegian olivine catalyst was tested for comparison to reported results [10–12]. At all temperatures, it demonstrated an activity lower than the Austrian catalyst, but higher than that of the N.C. one. Differences in syngas composition and space velocity between the reported results [10–12] and the present study would also lead to differences in conversion. Since the Norwegian catalyst was likely calcined before acquisition (mass specific surface area of 0.1 $m^2$/g which is much lower than the other fresh catalysts) and calcinations prior to the reaction increased $C_{10}H_8$ conversion [10–12], it is not further discussed. Rather, it was included to put the present results in context with available data in the literature.

As shown in Fig. 1, the more active catalysts for $C_{10}H_8$-$H_2O$ reforming were also more active for $CH_4$-$H_2O$ reforming. For the Austrian catalyst, $CH_4$ conversion was 12% during the hold at 900 °C and the surface area normalized reaction rate was near 15 μmol of $CH_4$ converted/$m^2$/s. Even though $CH_4$ conversion is low under all conditions and thus steam is supplied in excess, CO (and not $CO_2$) was the primary product.

In addition to untreated olivine catalysts, an Austrian olivine catalyst calcined in air at 1600 °C for 4 h was tested. The calcination caused close to a 10-fold loss of mass specific

Table 3
Specific surface areas (physical adsorption of Kr) and densities of olivine catalysts

| Catalyst | SSA ($m^2$/g) | Density (g/$cm^3$) |
|---|---|---|
| Wash. | 1.42 | 3.28 |
| N.C. | 0.86 | 3.23 |
| Austrian | 1.29 | 2.64 |
| Austrian-calcined | 0.15 | 3.25 |

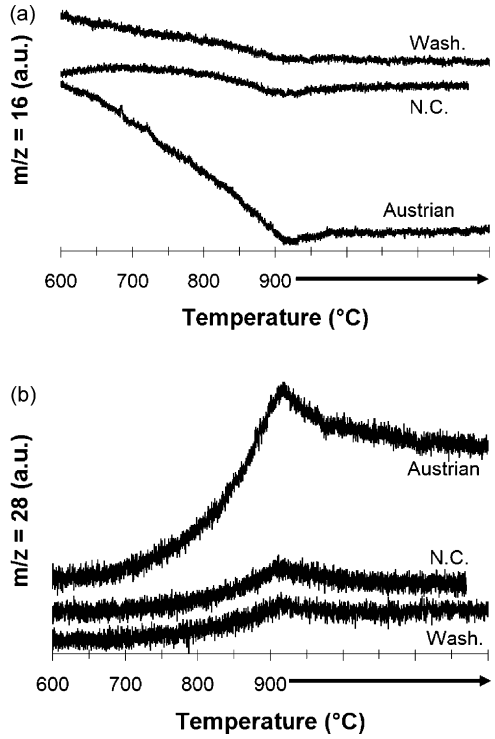


Fig. 1. Temperature-programmed methane steam reforming over olivine catalysts. Profiles for (a) methane, $m/z = 16$ and (b) carbon monoxide, $m/z = 28$. Profiles are offset for clarity.

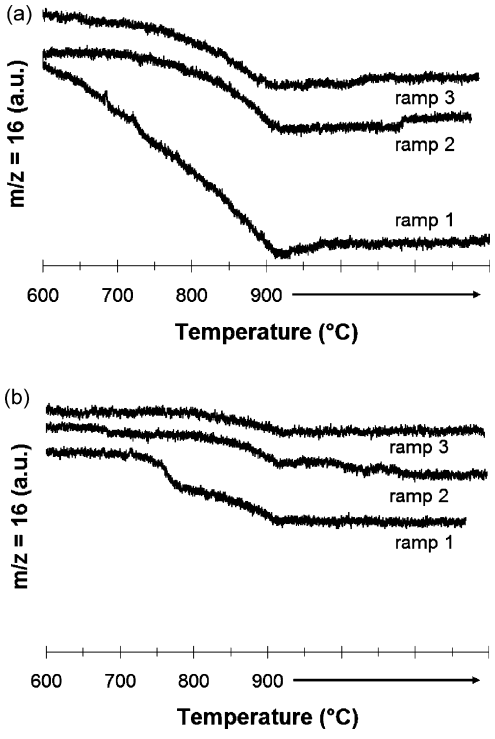


Fig. 2. Methane ($m/z = 16$) profiles for temperature-programmed methane-steam reforming over an (a) untreated Austrian olivine catalyst and (b) Austrian olivine catalyst calcined at 1600 °C for 4 h. Profiles are offset for clarity, but the same scale is used.

surface area (Table 3). Despite the significant loss in surface area, this catalyst demonstrated appreciable activity (Table 2) for $C_{10}H_8$ conversion (not a factor of 10 lower). Additionally, as shown in Fig. 2, this catalyst was tested for $CH_4$-$H_2O$ reforming. CO was the primary carbon-based product (not shown). $CH_4$ conversion decreased upon repeated cycling for both the untreated and calcined Austrian olivine catalysts. The N.C. and Wash. catalysts also showed decreasing activity during similar experiments (data not shown). The untreated Austrian catalyst demonstrated the largest decrease for $CH_4$ conversion. With the exception of the first ramp for the untreated Austrian sample (12%), $CH_4$ conversion was below 10% at 900 °C (scaling is the same in both parts of Fig. 2 to allow qualitative comparison).

### 3.2. Bulk structural characterization

A phase diagram of the MgO, FeO, and $SiO_2$ system is provided in Scheme 1 to aid on the discussion of the structural characterization. However, it should be used with caution because it fails to account for Fe in higher oxidation states and behavior under reaction and reducing conditions.

Elemental analyses were performed by ICP-MS for the three samples as shown in Table 4. The presence of several elements was detected at trace amounts (<1%) that are below the detection limits of other techniques (e.g., XRD). Following a procedure by Courson et al. [17,20,21] that assumed all Si and Mg are contained in the olivine structure (errors may exist since it ignores the presence of Mg and Si in phases other than olivine) and all components at small concentrations can be ignored, the Wash. and N.C. samples were deemed close to $(Mg_{0.918}Fe_{0.082})_2SiO_4$ and $(Mg_{0.925}Fe_{0.075})_2SiO_4$, respectively, with an extra 5% of $FeO_x$ species present to explain the excess Fe content. Results were similar to those reported for a presumably calcined Austrian olivine [17,20,21]. Analysis of the untreated Austrian olivine predicted a negative amount of $FeO_x$ species present meaning that Mg and Si likely existed in other species at appreciable quantities. Since the total did not come close to adding up to 100% as it did with the other

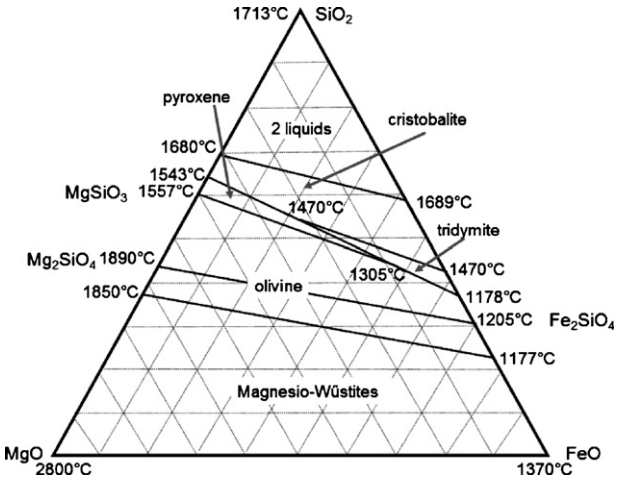


Scheme 1. Phase diagram (adapted from [46]) for crystalline phases of MgO, FeO, and $SiO_2$ mixtures.

Table 4
Elemental analyses (mass%) of olivine catalysts

| Element | Wash. | N.C. | Austrian | Austrian-calcined |
|---|---|---|---|---|
| Mg | 28.7 | 30.7 | 21.2 | 28.4 |
| Si | 18.2 | 19.4 | 16.5 | 20.6 |
| Fe | 5.9 | 5.7 | 5.2 | 6.9 |
| Ni | 0.3 | 0.2 | 0.1 | 0.3 |
| Al | 0.1 | 0.2 | 0.4 | 0.2 |
| Cr | 0.3 | 0.3 | 0.3 | 0.4 |
| Ca | 0.1 | 0.1 | 0.7 | 0.6 |
| Mn | 0.1 | 0.1 | 0.1 | 0.1 |
| Total on oxide basis | 96.3 | 101.9 | 85.4 | 102.8 |

samples, it also suggested that other elements existed in significant quantities.

A comparison of the elemental analyses for the calcined Austrian sample is also shown in Table 4. Due to the loss of $CO_2$ and $H_2O$ during calcination, the total was much closer to 100%. All of the secondary elements were present at similar levels. Like the untreated sample, the calcined sample contained more Mg and Fe relative to Si for all these elements to be present only in the olivine structure suggesting that secondary phases, particularly ones enriched in Si, may be present.

As shown in Fig. 3(a), XRD was performed to characterize the structure of the olivine phase and identify other phases present. From the diffraction patterns, olivine was the major crystalline phase present. Assuming Fe made up a relatively minor amount of the olivine phase, Miller indices were labeled

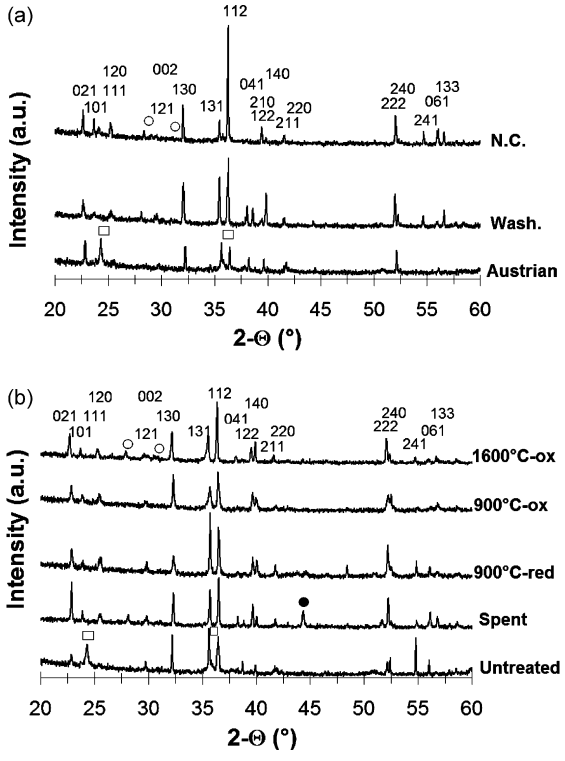


Fig. 3. XRD patterns for (a) different untreated olivine and (b) processed Austrian olivine catalysts where numerical values specify Miller indices for the olivine phase and other phases denoted as $MgSiO_3$ (○), $(Mg,Fe)_3Si_2O_5(OH)_4$ (□), and Fe (●). Data are offset for clarity.

using forsterite ($Mg_2SiO_2$) as an approximation (ICDD file #80-944). The phase was easily observed from many diffraction lines, but particularly by the strong diffraction of its (1 3 0), (1 3 1), and (1 1 2) planes. The only other phases detected were $MgSiO_3$ (ICDD file #71-786) and $(Mg,Fe)_3Si_2O_5(OH)_4$ (ICDD file #2-95). $MgSiO_3$ was strong in the N.C. and Wash. samples, but not in Austrian samples. For the Austrian sample, the main diffraction line for a serpentine or antigorite phase, $(Mg,Fe)_3Si_2O_5(OH)_4$, near 24.5° rivaled those of the olivine phase suggesting that a large portion of the sample was composed of this phase. The serpentine phase was observed previously for an unidentified olivine material [14]. Since several crystalline hydroxyl groups are contained in the structure, it helped explain the low elemental analysis total. It was also present to a lesser degree in the N.C. sample. Even though it has been reported [17,20,21] that calcined Austrian olivine samples contained free Fe oxide phases such as α-$Fe_2O_3$ (ICDD file #73-2234), γ-$Fe_2O_3$ (ICDD file #73-2234), $Fe_3O_4$ (ICDD file #65-3107), and $MgFe_2O_4$ (ICDD file #88-1936), this study did not observe these species. The latter three Fe oxide phases, which cannot be distinguished from each other by this technique, also have their main peak at 35.5° masked by the olivine (1 3 1) diffraction line and a secondary line for $(Mg,Fe)_3Si_2O_5(OH)_4$. Their secondary lines were not strong enough to imply their presence. Additionally, other free Mg species such as MgO (ICDD file #45-946) and $MgCO_3$ (ICDD file #8-479) were not detected.

Relative intensities of different olivine diffraction planes and peak positions were used as an indicator of the Fe incorporation into the olivine phase. Comparing forsterite (ICDD files #80-944 or 34-0189) to fayalite ($Fe_2SiO_2$, ICDD files #80-948 or 34-0178) as an example, intensity increases for the (1 3 0) line and decreases for the (1 3 1) line indicate more Fe relative to Mg in the olivine lattice. Moreover, diffraction lines are located at smaller angles (larger *d*-spacing and unit cell volume) when Fe is present. This shift is associated with $Fe^{+2,HS}$ (0.78 Å) having a larger crystal radius than $Mg^{+2}$ (0.72 Å) in octahedral coordination. Orthorhombic lattice parameters are given in Table 5. Using both of these techniques, the N.C. sample has more Fe in the olivine lattice than the Austrian and Wash. samples. For calcined Austrian catalysts, the unit cell volume has been used to quantify the composition of Fe and Mg in the olivine structure [17]. Using this approach, the composition of the olivine phase was determined to be $(Mg_{0.82}Fe_{0.18})_2SiO_2$, $(Mg_{0.88}Fe_{0.12})_2SiO_2$, and $(Mg_{0.93}Fe_{0.07})_2SiO_2$, for the N.C., Wash., and Austrian samples, respectively. With the exception of the Wash. sample, these values are significantly different from the structure arrived at from the elemental analyses and

Table 5
Orthorhombic unit cell parameters determined from XRD results in Fig. 3 for olivine catalysts

| Catalyst | *a* (Å) | *b* (Å) | *c* (Å) | *V* (Å$^3$) |
|---|---|---|---|---|
| Wash. | 4.767 | 10.237 | 5.994 | 292.51 |
| N.C. | 4.766 | 10.253 | 6.008 | 293.56 |
| Austrian | 4.757 | 10.226 | 5.995 | 291.59 |
| Austrian-calcined | 4.764 | 10.238 | 5.993 | 292.26 |
| Austrian-spent | 4.755 | 10.218 | 5.990 | 291.04 |

indicated the presence of other phases. Additional phases may not have been detected because of high dispersion, low concentrations, a lack of crystallinity (e.g., $SiO_2$ likely amorphous), or an overlap of diffraction lines with other phases.

To aid in the examination of different treatments, the Austrian sample was calcined and reduced at 900 °C for 2 h. These samples are labeled as 900 °C-ox and 900 °C-red, respectively. Diffraction patterns, presented in Fig. 3(b), showed that the serpentine phase decomposed during these treatments. $MgSiO_3$ was only detected for the spent catalyst and the sample calcined at 1600 °C. The main line for metallic Fe was also observed for the samples exposed to reducing conditions. While it was barely present in the sample reduced at 900 °C indicating relatively well-dispersed Fe particles, a sharp lined existed for the spent catalyst. Using Scherrer analysis, the crystallite size for metallic Fe in the spent sample was 21.4 nm.

Lattice parameters were calculated for the olivine phase and the results are also shown in Table 5. The sample amount was not enough for catalysts reduced and calcined at 900 °C so lattice parameters were not determined. Based on predictions from the unit cell volume, the catalyst calcined at 1600 °C had a formula of $(Mg_{0.90}Fe_{0.10})_2SiO_2$ while the spent catalyst's formula was $(Mg_{0.97}Fe_{0.03})_2SiO_2$. An increase of Fe in the olivine lattice during calcination came from free Fe being incorporated after it was released during the decomposition of the serpentine phase. However, when exposed to reducing conditions, Fe was freed by the decomposition of the serpentine phase and agglomerated into crystallites large enough to be detected by XRD. The claim was supported by the fact that the intensities for the (1 3 0) and (1 3 1) diffraction lines decreased and increased, respectively, indicating less Fe relative to Mg in the olivine structure. Under oxidizing conditions, the opposite trend with relative intensities occurred although to a lesser extent, suggesting a slight increase in Fe relative to Mg in the olivine structure.

Laser Raman spectra, as shown in Fig. 4, were acquired to complement the XRD data. Olivine was again a major species as indicated by several strong vibrations. Forsterite [22–25] and fayalite [22,23,25] olivine samples have been previously studied and have been used to identify the bands associated with the olivine structure in the present work. The vibrations near 822, 854, 881, 921, and 964 $cm^{-1}$ are caused by $SiO_4$ stretching. Also, a vibration for the symmetric deformation of $SiO_4$ was observed at 435 $cm^{-1}$ while other bands associated with the internal bending modes (between 400 and 700 $cm^{-1}$) of the $SiO_4$ ionic groups were not. At lower frequencies (<400 $cm^{-1}$), vibrations corresponded to $SiO_4$ rotation (305 $cm^{-1}$) and translation (226 $cm^{-1}$) and Mg or Fe translation (not detected). Changes in the wavenumber of a specific vibration is related to composition [22,25]. Raman shifts were the same for the Austrian and Washington samples and indicated 90% or more Mg and 10% or less Fe in the olivine phase. Vibrations occurred at a slightly lower wavenumber (1 or 2 $cm^{-1}$) for the N.C. sample so contained slightly more Fe in the olivine phase than in the other samples.

The other primary phase is the serpentine phase, which has also been studied previously by laser Raman spectroscopy [26–29]. The vibrations at 230, 355, 385, 477, 621, 680, 1090, and 1106 $cm^{-1}$ are expected for the serpentine phase. While the intensities of the serpentine phase were in agreement with the trend found by XRD (i.e., Austrian and Wash. samples have highest and lowest concentrations, respectively), it was interesting that the serpentine phase is much more intense than the olivine phase for the Austrian and N.C. samples. These differences may be related to spectroscopy being more surface sensitive than XRD. The vibration at 131 $cm^{-1}$ appeared linked to the serpentine phase, but the literature does not identify vibrations at this low of a Raman shift.

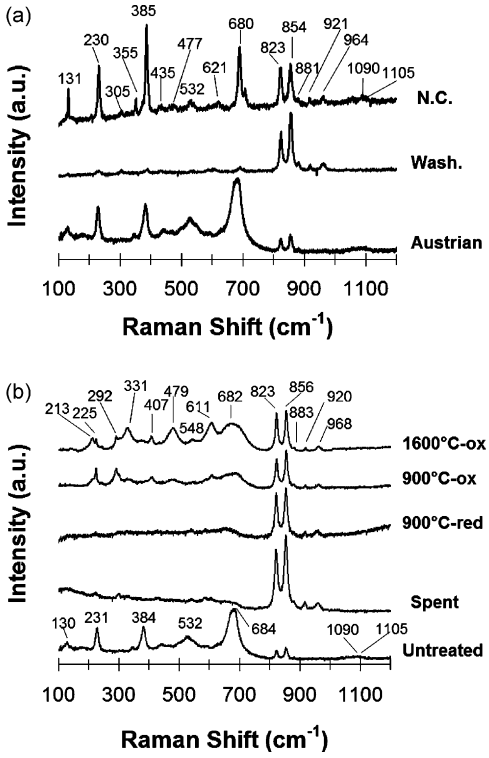


Fig. 4. Laser Raman spectra for (a) different untreated olivine and (b) processed Austrian olivine catalysts. Data are offset for clarity.

An advantage of characterizing these samples with vibrational spectroscopy is that compounds with similar structure (e.g., γ-$Fe_2O_3$, $Fe_3O_4$, and $MgFe_2O_4$) can be identified. For these three samples, Raman spectroscopy demonstrated that $Fe_3O_4$ may be present (primary vibrations at 307, 532, and 667 $cm^{-1}$ [30,31] but overlapped with others), but γ-$Fe_2O_3$ (primary vibrations at 665 and 721 $cm^{-1}$ [30,31]) and $MgFe_2O_4$ (primary vibrations at 333 $cm^{-1}$ [32]) were not. Additionally, α-$Fe_2O_3$ (primary vibrations at 223, 291, and 407 $cm^{-1}$ [30,31]), $SiO_2$ (primary vibrations at 975 for Si–OH and 1060 $cm^{-1}$ [33]), and $MgSiO_3$ (primary vibrations at 1011 and 1033 $cm^{-1}$ [34]) were not observed. Finally, $MgCO_3$ may exist as its strongest vibration (1094 $cm^{-1}$ [35]) overlapped with one for the serpentine phase.

As shown in Fig. 4(b), only the olivine phase was observed for the reduced and spent catalysts whereas α-$Fe_2O_3$ appeared after oxidizing treatments. The bands at 213, 292, and 407 $cm^{-1}$ [30,31] are associated with it. Even after the

calcination at 1600 °C, the serpentine phase was still detected. Also under oxidizing conditions, bands at 213, 331, and 548 confirmed the formation of $MgFe_2O_4$.

The catalysts were also characterized by ATR-IR and the results are shown in Fig. 5. In the high wavenumber region, all samples possessed a band for the hydroxyl stretching near 3685 $cm^{-1}$. The hydroxyl groups in the serpentine phase have strong signals with the major stretching band near 3675 $cm^{-1}$ [36]. The intensity was largest for the untreated sample both before and after $C_{10}H_8$-$H_2O$ reforming. The intensity decreased, indicating serpentine decomposition, more under reducing than oxidizing conditions and also decreased more as the calcination temperature increased. For the spent sample, the intensity obtained was higher than expected. This result may be caused by interactions that formed due to $H_2O$ being present during the reaction and remained during cooling. The region for Si–O vibrations is shown in Fig. 5(b). Serpentine has Si–O vibrations at 1076, 990, and 972 $cm^{-1}$ [36] while Mg-based olivine has vibrations at 841, 892, 956, 983, and 1001 $cm^{-1}$ [37]. For a Fe-based olivine, the vibration shifted to roughly a 50 $cm^{-1}$ lower frequency [37]. Using these studies, the band at 903 $cm^{-1}$ is linked to Si–O vibrations in the olivine structure whereas the band at 985 $cm^{-1}$ is associated to the same vibration for the serpentine phase. Several shoulders on these peaks existed and were attributed to the other Si–O bands listed above. Vibrations near 1000 and 955 $cm^{-1}$ appeared responsible for the complex shape of the sample calcined at 1600 °C in air. Similar behavior was detected for the sample reduced at 900 °C while a simpler spectrum was observed for the sample calcined at 900 °C. Thus, the data agreed with previous results that the serpentine phase decomposed more easily under reducing than oxidizing conditions. This assertion is indicated by the decreased intensity of bands for the serpentine phase near 1076 and 972 $cm^{-1}$ while bands like the one near 841 $cm^{-1}$ for the olivine phase increased.

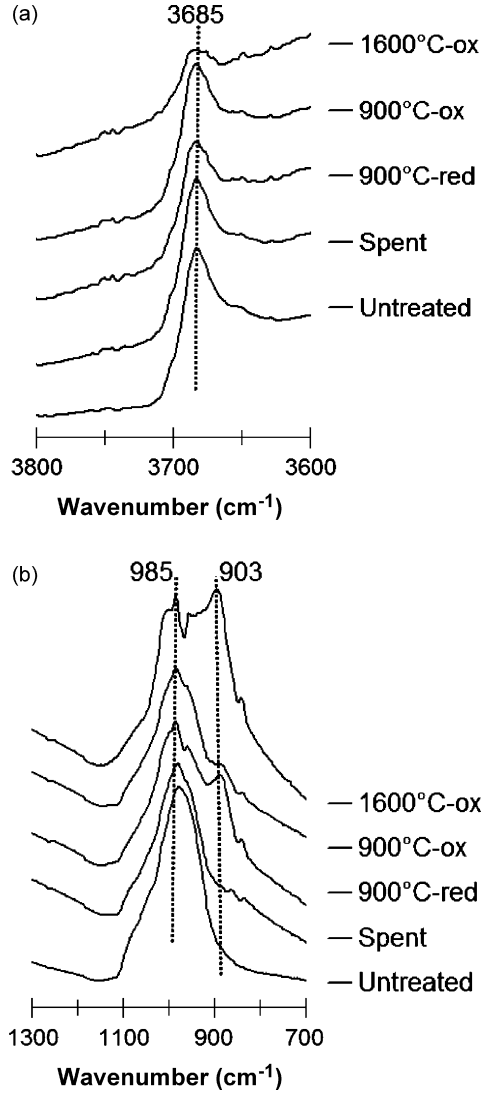


Fig. 5. Structural characterization of processed Austrian olivine catalysts by ATR-IR spectroscopy. (a) OH region and (b) Si–O region. Spectra are offset for clarity.

### 3.3. Temperature-programmed studies

Since the untreated catalysts contained phases with hydroxyl groups and perhaps also ones with carbonate species, thermal treatments were performed to monitor the evolution of these species which are unstable at elevated temperatures. Profiles are shown in Fig. 6 where $H_2O$ ($m/z$ = 18) and $CO_2$ ($m/z$ = 44) were the only species detected. For each sample, $H_2O$ formed over a wide temperature range with a maximum near 700 °C. Moreover, the intensities of $H_2O$ signals followed the trend established by the structural studies for the amount of the serpentine phase. The amount of $CO_2$ evolution also followed the same pattern. Since the formation of $MgCO_3$ and $SiO_2$ has been studied by reacting serpentine phases with $CO_2$ for potential sequestration applications [38,39], it was inferred that the $CO_2$ was linked to $MgCO_3$. The evolution of species, especially $H_2O$, from the calcined Austrian sample was small compared to the untreated samples.

To further investigate the stability of the serpentine phase under reducing conditions, the reduction behavior of the untreated sample was monitored by in situ XRD. The results as a function of temperature under reducing conditions are shown in Fig. 7. The serpentine phase was specified by its broad diffraction lines near 24.5 and 35.8°. As temperature increased,

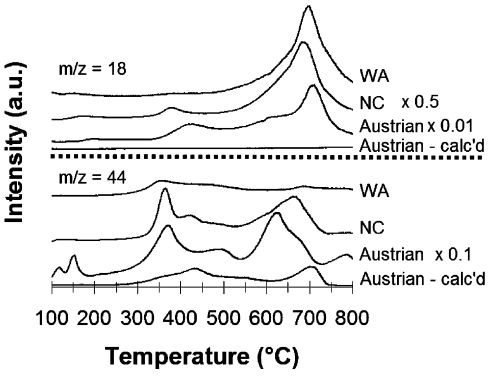


Fig. 6. Profiles for olivine catalysts during thermal treatments under an inert environment. Profiles are offset for clarity.

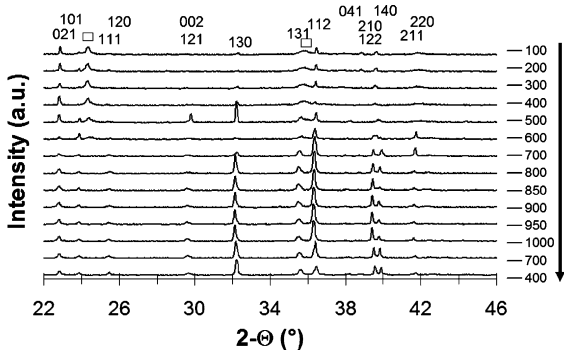


Fig. 7. In situ diffraction patterns during the reduction (5% $H_2/N_2$) of the untreated Austrian olivine catalyst. Patterns are offset for clarity with the arrow indicating chronological order. $(Mg,Fe)_3Si_2O_5(OH)_4$ is denoted as □.

all lines shifted towards lower angles as the lattice thermally expanded. Additionally, lines for the serpentine phase began to decrease above 400 °C and were no longer detected at 700 °C. Several transformations regarding Fe (suggesting Fe in the serpentine structure) were detected in this temperature range before the structure becomes stable at higher temperatures. At 500 °C, the line near just below 30° showed the presence of a spinel phase (i.e., γ-$Fe_2O_3$, $Fe_3O_4$, or $MgFe_2O_4$). A sharp increase in the (1 3 0) olivine diffraction line also confirmed interactions of the Fe with the olivine phase. At 600 and 700 °C, a line appeared at 42° which implied the presence of FeO while the changes associated with the spinel and Fe in olivine were no longer present. Above 700 °C, FeO disappeared and Fe likely associated to the olivine structure or formed finely dispersed metal particles. The structural changes were irreversible under reducing conditions as the changes did not repeat when the temperature was lowered.

Sequential reduction–oxidation studies were performed on the three untreated samples and the results are shown in Fig. 8. $H_2$ consumption is much greater for the Austrian sample than for the other samples. Similarly, the Austrian sample consumed much more oxygen than the other samples to re-oxidize these species. In a second cycle (not shown), the Austrian sample showed very similar reduction and oxidation profiles as the first cycle whereas the Wash. and N.C. samples demonstrated profiles similar to the first cycle for N.C. sample. Thus, the Austrian sample contained much more available Fe species than the others. The profiles were very different than results for untreated Norwegian olivine catalysts which showed no reduction occurred [10], but showed similar reduction profiles to untreated Austrian olivine catalysts [21]. The primary difference was that the first reduction feature occurred at a lower temperature. The first reduction feature was caused by the reduction of the serpentine phase as demonstrated by the in situ XRD results. The intensity of the first reduction feature scaled with the amount of serpentine phase present in the samples. Upon re-oxidation, a low temperature peak was only observed for the Austrian sample, which suggested that the serpentine phase in it contained more Fe than did the serpentine phase in the N.C. sample. The reduction feature near 950 °C is associated with the reduction of Fe in the olivine phase while the intermediate one (650–800 °C) was linked to the reduction of $Fe_3O_4$.

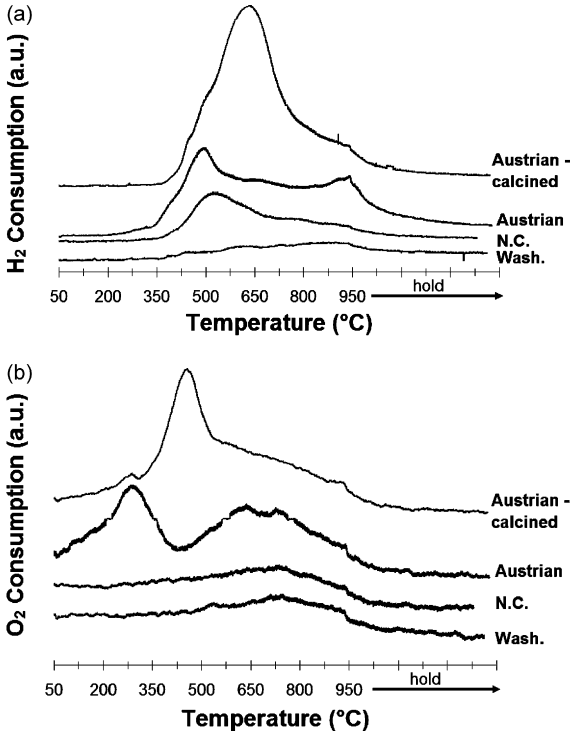


Fig. 8. Sequential (a) TPR and (b) TPO for the olivine catalysts. Profiles are offset for clarity.

Reduction–oxidation behavior of the untreated and calcined samples was also compared in Fig. 8. The low temperature reduction was attributed to the reduction of α-$Fe_2O_3$. Owing to the free Fe being more oxidized, the amount of $H_2$ consumed was much greater for the calcined sample. Since the $H_2$ consumption was much greater (more than 13% expected for the increase in the oxidation state of Fe), it appears that the calcination allowed increased access for $H_2$ to reach the free Fe oxide species. That is, even though some free Fe entered into the olivine structure (noticed by a slight increase in the reduction above 900 °C), the remaining Fe is more easily reduced despite an overall decrease in its amount. During the oxidation, a single oxidation peak occurred for the calcined catalyst indicating the calcination leads to different reduction–oxidation behavior. A second reduction–oxidation cycle (data not shown) was performed and it demonstrated similar profiles. The behavior was very different than that previously reported for Austrian olivine catalysts [20,21]. Differences may be due to two different reducible Fe species, one for $Fe_3O_4$ and another Fe decomposed from the serpentine phase, in the untreated sample while the high temperature calcination caused the two species to form a single phase.

### 3.4. Surface characterization

Surfaces of the three samples were examined using XPS and the individual region scans are shown in Fig. 9. Trace elements (e.g., Mn, Cr, Ni, Al., etc.) were not detected meaning that these species did not exist in appreciable concentrations near the surface. The Mg 1s (not shown) and 2p peaks aligned in the general range of divalent Mg [40] and there were not significant

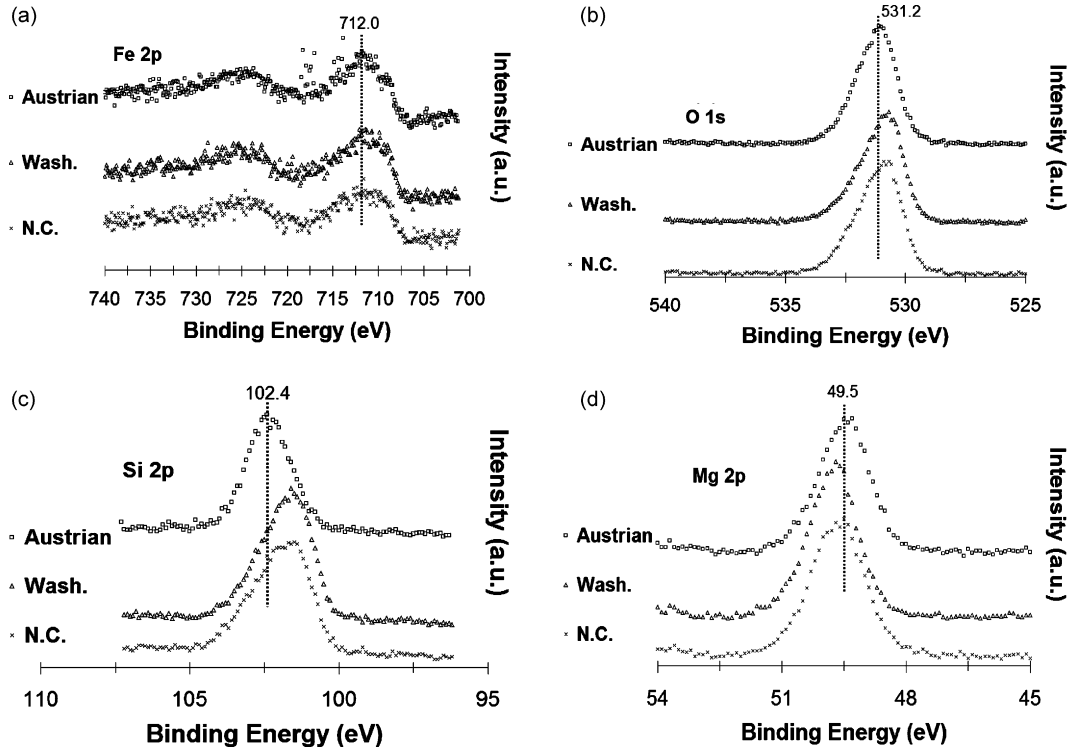


Fig. 9. Region of the XPS spectra for (a) Fe 2p, (b) O 1s, (c) Si 2p and (d) Mg 2p. Spectra are offset for clarity.

differences among the samples. The location of the Fe 2p peak (712 eV) agreed with spectra acquired for Norwegian olivine [10]. The O 1s peak (531.2 eV) fit into the range for the olivine phase, but the peaks for metal oxide and carbonate species are in this general range [40]. The Si 2p peak coincided with the silicate region as would be expected [40]. In general, the peak locations did not shift very much for the different samples. The Austrian sample did show slightly higher binding energies for O 1s and Si 2p peaks, which was caused by the increased concentrations of hydroxides and carbonates.

The primary differences between the samples were associated to the surface compositions as revealed in Table 6. Fe was present at a higher concentration in the Austrian catalyst. The Wash. catalyst was much less oxidized at the surface in comparison to the other catalysts. The amount of oxygen at the surface could be linked to different phases with varying elemental compositions. For example, oxygen is more prevalent in carbonates or the olivine structure than in base metal oxides.

The Austrian olivine catalyst was characterized as a function of treatment using XPS. Individual region spectra (not shown) were similar to the untreated Austrian olivine spectra shown in Fig. 9. The Mg 1s and 2p peaks were in identical positions. Peaks for the other regions shifted to slightly lower binding energies under all processing conditions. For the calcined samples, the shift was 1 eV for the Fe 2p and Si 2p peaks and 0.5 eV for the O 1s peak. Shifts were slightly less under reducing conditions and occurred largely due to the serpentine decomposition (though loss of carbonates may have influenced O 1s shift). Surface compositions for these samples were also presented in Table 6. Comparing the two treatments at 900 °C, the amount of Fe at the surface decreased under reducing conditions while it remained the same during oxidizing conditions. However, the higher calcination temperature also led to loss of Fe at the surface. Fe clustered into large particles

Table 6
Surface composition measured by XPS for the olivine catalysts

| Catalyst | Region | B.E. (eV) | Composition (%) |
|---|---|---|---|
| Wash. | Fe $2p_{3/2}$ | 711.0 | 1.6 |
| | O 1s | 531.0 | 63.8 |
| | Si 2p | 101.8 | 15.3 |
| | Mg 2p | 49.8 | 19.3 |
| N.C. | Fe $2p_{3/2}$ | 711.2 | 1.5 |
| | O 1s | 531.4 | 65.0 |
| | Si 2p | 102.0 | 14.5 |
| | Mg 2p | 49.7 | 19.0 |
| Austrian | Fe $2p_{3/2}$ | 711.4 | 2.0 |
| | O 1s | 531.2 | 65.7 |
| | Si 2p | 102.4 | 13.9 |
| | Mg 2p | 49.5 | 18.3 |
| Austrian reduced 900 °C | Fe $2p_{3/2}$ | 710.8 | 1.4 |
| | O 1s | 531.1 | 64.0 |
| | Si 2p | 102.0 | 16.3 |
| | Mg 2p | 49.9 | 18.3 |
| Austrian calcined 900 °C | Fe $2p_{3/2}$ | 710.6 | 2.1 |
| | O 1s | 530.8 | 63.9 |
| | Si 2p | 101.7 | 15.4 |
| | Mg 2p | 49.8 | 18.6 |
| Austrian calcined 1600 °C | Fe $2p_{3/2}$ | 710.7 | 1.6 |
| | O 1s | 530.8 | 59.7 |
| | Si 2p | 101.6 | 14.2 |
| | Mg 2p | 49.8 | 24.4 |

under reducing conditions, decreasing the amount of Fe at the surface.

## 4. Discussion

Catalytic activity differences as the origin of the olivine and treatments changed are explained by physiochemical property differences. Results also support Fe as being important for the catalytic activity in olivine catalysts. Finally, remarks on the application of these materials for tar removal in FB gasifiers are made based on the catalytic activity and stability.

### 4.1. Effect of olivine origin

The untreated Austrian olivine catalyst demonstrated the highest $C_{10}H_8$- and $CH_4$-$H_2O$ reforming activity while the Wash. catalyst showed the lowest activity for the same reactions. The Austrian sample had the lowest amount of Fe in the olivine structure, but the highest amount of secondary phases. Since Fe was likely present in the secondary phases for the Austrian catalyst, the formula predicted by the lattice parameters, $(Mg_{0.93}Fe_{0.07})_2SiO_4$, seemed appropriate. The main secondary phase was the serpentine phase, which was more easily detected by Raman spectroscopy than XRD. Since Raman spectroscopy is more surface sensitive than XRD, the data implied that the serpentine phase was more prevalent near the surface, which would be in agreement with the results from XPS that showed more Fe at the surface for the Austrian sample. Thus, it is hypothesized that a Fe-bearing serpentine phase was located near surface in the Austrian sample and, upon its decomposition at elevated temperature, free Fe deposited on the surface and was responsible for its higher catalytic activity. Since the Austrian catalyst showed such unique behavior due to this decomposition under reaction conditions, the decomposition of serpentine phase was examined under various conditions.

Since Fe is present in equal amount at the surface, it is more difficult to explain activity differences between the Wash. and N.C. olivine catalysts. While the N.C. olivine sample had a greater amount of secondary phases including the serpentine phase (XRD and Raman spectrum showed the amount was less than in the Austrian catalyst), elemental analysis and XPS results indicated that Fe behaved differently in this sample than in the Austrian one. The Wash. olivine sample had a limited amount of other phases in significant quantities and the various techniques were found in agreement for an olivine composition near $(Mg_{0.9}Fe_{0.1})_2SiO_4$. Since the concentration of Fe in the total material (elemental analysis) and at the surface (XPS) was similar, the chemical environment of Fe must be important. Lattice parameters indicated that the olivine phase in the N.C. catalyst has a higher Fe concentration in it than in the olivine phase for the Wash. catalyst. Thus, Fe is expected to reside almost exclusively in the olivine phase for the N.C. catalyst whereas free Fe oxide is also present in the Wash. catalyst. From these claims, it is inferred that the Fe-rich olivine phase (N.C. catalyst) is more active than the combination of an olivine phase with less Fe and free Fe oxide species (Wash. catalyst). In addition to differences in the reforming activity of the different phases, secondary effects may also play a role. Increased Fe concentration causes the expansion of the unit cell, which would cause more space between metal sites. Structural differences may also arise from preferential occupation of the unequal metal sites in olivine. For example, Ni [41] and Fe [22] preferentially filled olivine's M1 position at low concentrations (the limit is also influenced by temperature) while the occupancy became random at higher concentrations. Thus, it is speculated that cationic distribution may exist between the two samples and it may lead to differences in catalytic activity.

### 4.2. Effect of treatments

The calcined catalyst showed much lower hydrocarbon conversions for $C_{10}H_8$ and $CH_4$-$H_2O$ reforming than the untreated catalyst. However, after accounting for surface area differences, the calcined sample yielded a higher rate of reaction. Since exposure to oxidizing environments at high temperature led to more Fe in the olivine structure, it supported earlier evidence that Fe in the olivine phase is more active than free Fe oxide species. On the other hand, exposure to reducing or $C_{10}H_8$-$H_2O$ reforming conditions caused Fe to be reduced out of the olivine structure and Fe agglomerated into large particles over time. These differences were due to the decomposition of a surface-enriched Fe-bearing serpentine phase, which was not thermally stable and explained for the mass loss for the untreated Austrian olivine catalyst during 48 h on stream. The serpentine phase decomposed much more readily under reducing atmospheres compared to oxidizing ones and the nature of the initial treatment led to vastly different reduction–oxidation profiles indicating Fe interacted differently with the olivine under reducing conditions such as in syngas depending on whether it was initially reduced or oxidized. Thus, the nature of the initial treatment was proven to be very important towards the behavior and catalytic properties. An initial calcination helped disperse Fe through the formation of $\alpha$-$Fe_2O_3$ and Fe in the olivine structure whereas metallic Fe aggregates formed under simulated syngas and reducing conditions.

### 4.3. Fe species as the active site

Thus far, Fe was assumed to be involved in the active site for the reactions. The assumption was made because previous studies on olivine catalysts demonstrated correlations between Fe and catalytic activity [10,11,14]. Additionally, the results of the present study support these claims. Catalysts with the most surface Fe and greatest reducibility were the most active. These results support metallic Fe, which is expected to be more active for C–C and C–H bond making and breaking than oxide phases, being involved as a site with high activity. Moreover, analysis of one of the more active catalysts following $C_{10}H_8$-$H_2O$ reforming indicated metallic Fe agglomeration, which may explain deactivation (as discussed in Section 4.4, coking may also be operative) during simulated TOS for $CH_4$-$H_2O$ reforming due to decreased metallic Fe dispersion.

### 4.4. Potential of these materials for FB gasifier applications

Even the best performing catalyst showed incomplete $C_{10}H_8$ conversion below 900 °C and low $CH_4$ conversion at 900 °C indicating more active catalysts are needed. It is especially true in applications where hydrocarbon-free syngas is desired since the activity for $CH_4$ removal was too low to eliminate the need for a second post-gasifier reactor. Additionally, deactivation may also limit the application of these materials. Deactivation was observed during repeated $CH_4$-$H_2O$ reforming experiments and may be caused by the growth of Fe clusters that decrease dispersion and/or by coke formation (SSA of 8.5 $m^2$/g measured for untreated Austrian olivine after $C_{10}H_8$-$H_2O$ reforming). While coking may be allayed by the use of a dual bed FB gasifier, long-term stability of these materials remains questionable. For these reasons, addition of Ni by thermal impregnation (TI) is examined in future work [42] as a method for improving the catalytic activity and stability of olivine catalysts. Ni-olivine catalysts prepared by incipient wetness impregnation (IWI) need high temperature calcinations (1100 °C) to optimize performance for $CH_4$-$H_2O$ reforming [8,9], dry $CH_4$ reforming [8,20,21], toluene-steam reforming [9,43–45], and benzene-steam reforming [45] so alternative high temperature synthesis methods may help improve the formulation.

## 5. Conclusions

The origin of olivine catalysts and treatments prior to catalytic tests influenced the activity for $C_{10}H_8$ and $CH_4$-$H_2O$ reforming. The phase in which Fe was present and its location played a strong role in understanding the differences in catalytic activity. Of the secondary phases, Fe-bearing serpentine phase enriched at the surface was judged to be the most important for achieving high catalytic activity. When it decomposed, free Fe deposited on or near the surface. The nature of the initial thermal treatment also had a vital influence over the catalytic activity and physiochemical properties. Results support that Fe is involved in the active site. Due to poor $CH_4$-$H_2O$ reforming activity and potentially deactivation due to both carbon deposition and loss of Fe dispersion, improvements in activity and stability of these materials are needed. The present work, which focused on the catalytic and physiochemical property differences of the supports, constitutes the first phase of a more comprehensive study to evaluate Ni-olivine catalysts prepared by thermal impregnation.

## Acknowledgments

DOE funding under grant #DE-FG36-04GO14314 is gratefully acknowledged. Additional financial support was provided by the Ohio Department of Development through a Wright Center of Innovation. The authors would also like to acknowledge NSF for XPS under NSF-DMR grant #0114098.

## References

[1] G.W. Huber, S. Iborra, A. Corma, Chem. Rev. 106 (2006) 4044.
[2] L. Devi, K.J. Ptasinski, F.J.J.G. Janssen, Biomass Bioenergy 24 (2003) 125.
[3] C. Pfeifer, R. Rauch, H. Hofbauer, Ind. Eng. Chem. Res. 43 (2004) 1634.
[4] T.A. Milne, N. Abatzoglou, R.J. Evans, U.S. DOE NREL Report NREL/TP 570-25357 (1998) 1.
[5] D. Dayton, U.S. DOE NREL Report NREL/TP-510-32815 (2002) 1.
[6] Z. Abu El-Rub, E.A. Bramer, G. Brem, Ind. Eng. Chem. Res. 43 (2004) 6911.
[7] D. Sutton, B. Kelleher, J.R.H. Ross, Fuel Process. Technol. 73 (2001) 155.
[8] C. Courson, E. Makaga, C. Petit, A. Kienneman, Catal. Today 63 (2000) 427.
[9] D. Swierczynski, C. Courson, L. Bedel, A. Kiennemann, J. Guille, Chem. Mater. 18 (2006) 4025.
[10] L. Devi, M. Craje, P. Thune, K.J. Ptasinski, F.J.J.B. Janssen, Appl. Catal. A: Gen. 294 (2005) 68.
[11] L. Devi, K.J. Ptasinski, F.J.J.B. Janssen, Fuel Process. Technol. 86 (2005) 707.
[12] L. Devi, K.J. Ptasinski, F.J.J.B. Janssen, Ind. Eng. Chem. Res. 44 (2005) 9096.
[13] S. Rapagna, N. Jand, A. Kiennemann, P.U. Fuscolo, Biomass Bioenergy 19 (2000) 187.
[14] R. Rauch, K. Bosch, H. Hofbauer, D. Swierczynski, C. Courson, A. Kiennemann, Science in Thermal and Chemical Biomass Conversion Conference, Victoria BC, 2004.
[15] J. Corella, J.M. Toledo, R. Padilla, Energy Fuels 18 (2004) 713.
[16] L. Devi, K.J. Ptasinski, F.J.J.B. Janssen, S.V.B. van Paasen, P.C.A. Bergman, J.H.A. Kiel, Renew. Energy 30 (2005) 565.
[17] D. Swierczynski, C. Courson, L. Bedel, A. Kiennemann, S. Vilminot, Chem. Mater. 18 (2006) 897.
[18] L.G. Felix, D. Rue, R.B. Slimane, Engineering tar-cracking catalysts to optimize biomass gasification, in: 6th Internation Symposium on Gas Cleaning at High Temperatures, Osaka, Japan, 2005.
[19] L.G. Felix, R.B. Slimane, D.M. Rue, C.W. Choi, Engineering tar-cracking catalysts to optimize biomass gasification, in: The 14th European Biomass Conference and Exhibition, Paris France, 2005.
[20] C. Courson, L. Udron, D. Swierczynski, C. Petit, A. Kienneman, Sci. Technol. Adv. Mater. 3 (2002) 271.
[21] C. Courson, L. Udron, D. Swierczynski, C. Petit, A. Kienneman, Catal. Today 76 (2002) 75.
[22] B.A. Kolesov, J.V. Tanskaya, Mater. Res. Bull. 31 (1996) 1035.
[23] B.A. Kolesov, C.A. Geiger, Phys. Chem. Miner. 31 (2004) 142.
[24] C.C. Lin, J. Solid State Chem. 157 (2001) 102.
[25] K.E. Kuebler, B.L. Jolliff, A. Wang, L.A. Haskin, Geochim. Cosmochim. Acta 70 (2006) 6201.
[26] I.R. Lewis, N.C. Chafflin, M.E. Gunter, P.R. Griffiths, Spectrochim. Acta: Part A 52 (1996) 315.
[27] J.P. Perrillat, I. Daniel, K.T. Koga, B. Reynard, H. Cardon, W.A. Crichton, Earth Planet. Sci. Lett. 236 (2005) 899.
[28] D. Bard, B. Tylee, K. Williams, J. Yarwood, J. Raman Spectrosc. 35 (2004) 541.
[29] A.L. Auzende, I. Daniel, B. Reynard, C. Lemaire, F. Guyot, Phys. Chem. Miner. 31 (2004) 269.
[30] M.A. Legodi, D. de Waal, Dyes Pigments 74 (2007) 161.
[31] I. Chamritski, G. Burns, J. Phys. Chem. B 109 (2005) 4965.
[32] Z. Wang, P. Lazor, S.K. Saxena, H.S.C. O'Neil, Mater. Res. Bull. 37 (2002) 1589.
[33] D.K. Keller, T. Visser, F. Soulimani, D.C. Koningsberger, B.W. Weckhuysen, Vib. Spectrosc. 43 (2007) 140.
[34] C.C. Lin, J. Phys. Chem. Solids 66 (2004) 913.
[35] H.G.M. Edwards, S.E.J. Villar, J. Jehlicka, T. Munshi, Spectochim. Acta Part A 61 (2005) 2273.
[36] J.L. Post, L. Borer, Appl. Clay Sci. 16 (2000) 73.
[37] A.M. Hofmeister, Phys. Chem. Miner. 24 (1997) 535.

[38] R.K. Schulze, M.A. Hill, R.D. Field, P.A. Papin, R.J. Hanrahan, D.D. Byler, Energy Convers. Manage. 45 (2004) 3169.
[39] A.A. Park, L.-S. Fan, Chem. Eng. Sci. 59 (2004) 5241.
[40] J.F. Moulder, W.F. Stickle, P.E. Sobol, K.D. Bomben, Handbook of X-ray Photoelectron Spectroscopy, second ed., Perkin-Elmer Corporation, Eden Prairie, MN, 1992.
[41] C.M.B. Henderson, S.A.T. Redfern, R.I. Smith, K.S. Knight, J.M. Charnock, Am. Mineral. 86 (2001) 1170.
[42] J.N. Kuhn, Z. Zhao, A. Senefeld-Naber, L.G. Felix, R.B. Slimane, C.W. Choi, U.S. Ozkan, Appl. Catal. A: Gen., in press.
[43] D. Swierczynski, S. Libs, C. Courson, A. Kiennemann, Appl. Catal. B: Environ. 74 (2007) 211.
[44] D. Swierczynski, C. Courson, L. Bedel, A. Kiennemann, Chem. Eng. Process., in press.
[45] R. Zhang, Y. Wang, R.C. Brown, Energy Convers. Manage. 48 (2007) 68.
[46] N.L. Bowen, J.F. Schairer, Am. J. Sci. 29 (1935) 151.